

# Journal of Materials Chemistry A

Accepted Manuscript



This is an *Accepted Manuscript*, which has been through the Royal Society of Chemistry peer review process and has been accepted for publication.

*Accepted Manuscripts* are published online shortly after acceptance, before technical editing, formatting and proof reading. Using this free service, authors can make their results available to the community, in citable form, before we publish the edited article. We will replace this *Accepted Manuscript* with the edited and formatted *Advance Article* as soon as it is available.

You can find more information about *Accepted Manuscripts* in the [Information for Authors](#).

Please note that technical editing may introduce minor changes to the text and/or graphics, which may alter content. The journal's standard [Terms & Conditions](#) and the [Ethical guidelines](#) still apply. In no event shall the Royal Society of Chemistry be held responsible for any errors or omissions in this *Accepted Manuscript* or any consequences arising from the use of any information it contains.

## ARTICLE

# Electronic Structure and Photocatalytic Activity of Wurtzite Cu–Ga–S Nanocrystals and their Zn Substitution

Cite this: DOI: 10.1039/x0xx00000x

Tarek A. Kandiel<sup>a, b</sup>, Dalaver H. Anjum<sup>c</sup>, Philippe Sautet,<sup>d</sup> Tangui Le Bahers,<sup>d</sup> and Kazuhiro Takanabe<sup>a\*</sup>

Received 00th January xxxx,  
Accepted 00th January xxxx

DOI: 10.1039/x0xx00000x

www.rsc.org/

Stoichiometric and gallium-rich wurtzite Cu–Ga–S ternary nanocrystals were synthesized via a facile solution-based hot injection method using 1-dodecanethiol as a sulfur source. Use of 1-dodecanethiol was found to be essential not only as a sulfur source but also as a structure-directing reagent to form the metastable wurtzite structure. In addition, the substitution of zinc in the wurtzite gallium-rich Cu–Ga–S nanocrystals was also investigated. The obtained nanocrystals were characterized by X-ray diffraction (XRD), X-ray photoelectron spectroscopy (XPS), transmission electron microscopy (TEM), diffuse reflectance spectroscopy (DRS), photoluminescence (PL), and inductively coupled plasma atomic emission spectroscopy (ICP-OES). Electronic structures of pristine and Zn-substituted Cu–Ga–S system were investigated using density functional theory (DFT) with HSE06 exchange-correlation functional. The calculated bandgaps accurately reflect the measured ones. The allowed electronic transitions occur upon the photon absorption from the (Cu + S) band towards the (Ga + S) one. The Zn substitution was found not to contribute to the band edge structure and hence altered the bandgaps only slightly, the direct transition nature remaining unchanged with the Zn substitution. The photocatalytic activities of H<sub>2</sub> evolution from an aqueous Na<sub>2</sub>S/Na<sub>2</sub>SO<sub>3</sub> solution under visible-light illumination on the synthesized nanocrystals were investigated. While the stoichiometric CuGaS<sub>2</sub> exhibited negligible activity, the gallium-rich Cu–Ga–S ternary nanocrystals displayed reasonable activity. The optimum Zn substitution in the gallium-rich Cu–Ga–S ternary nanocrystals enhanced the H<sub>2</sub> evolution rate, achieving apparent quantum efficiency of >6% at 400 nm.

## Introduction

Hydrogen (H<sub>2</sub>) derived from renewable energy sources is considered the energy carrier of the future; therefore, the development of green technologies for its production is important. One of the proposed technologies is photocatalysis.<sup>1–3</sup> To utilize solar energy, a photocatalyst that can absorb visible light (>400 nm) should be developed. Cu–Ga–S ternary compounds can absorb light up to 550 nm, which makes them good candidates as visible-light responsive photocatalysts.<sup>4</sup> To enhance the H<sub>2</sub> production rate and reduce the photocorrosion commonly observed for sulfur containing photocatalysts, a S<sup>2–</sup>/SO<sub>3</sub><sup>2–</sup> solution has been employed.<sup>5,6</sup> S<sup>2–</sup> reagents irreversibly react with the photogenerated holes to produce polysulfides typically, and the photogenerated electrons promote the H<sub>2</sub> evolution reaction.<sup>1</sup> In fact, the photocatalytic H<sub>2</sub> production employing sacrificial reagents can be converted into a practical application, provided that a highly active visible-light photocatalyst is identified. For example, recovery of H<sub>2</sub> via photocatalysis for oxidation of hydrogen sulfide (H<sub>2</sub>S) would be of great economic and environmental interests. Many CdS-based photocatalysts have been employed and thoroughly investigated since the 1980s,<sup>7–17</sup> and the ternary and the quaternary metal sulfides have been recently investigated,

providing additional variety in selection of elements and resultant tunable bandgaps.<sup>18–31</sup>

The synthesis of ternary copper gallium sulfide-based nanocrystals has attracted much attention in recent years because they are more environmentally benign than their Cd- or Pb-based counterparts.<sup>21</sup> Moreover, they have a promising potential for many applications such as photovoltaic, light-emitting devices, radiation detection, and photocatalysis.<sup>4,29</sup> Commonly, ternary Cu–Ga–S materials with the thermodynamically preferred chalcopyrite crystal structure, which contains an ordered array of cations in the sublattice positions, are encountered during the synthesis.<sup>23,26,32</sup> The synthesis of wurtzite Cu–Ga–S nanocrystals remains challenging because of its metastable structure.<sup>29,30</sup> In this work, stoichiometric CuGaS<sub>2</sub> and gallium-rich nanocrystals were synthesized by employing a facile hot injection method: the recently-reported technique for CuIn<sub>x</sub>Ga<sub>1–x</sub>S<sub>2</sub>,<sup>27</sup> and CuGa<sub>2</sub>In<sub>3</sub>S<sub>8</sub> nanocrystals.<sup>31</sup> Especially Wang et al. successfully synthesized the monodisperse wurtzite CuIn<sub>x</sub>Ga<sub>1–x</sub>S<sub>2</sub> nanocrystal including stoichiometric CuGaS<sub>2</sub>.<sup>27</sup> Unlike the ordered chalcopyrite crystal structure, the wurtzite phase is disordered, and the Cu and Ga cations are randomly distributed in the cation sublattice;<sup>30</sup> consequently, the substitution of metal ions in the cation sublattice might be facile. Our

approaches include the substitution of Zn in the Cu-Ga-S nanocrystals to tune the defect amounts and bandgaps. Combining experiments and DFT calculation, effects of Zn substitution on electronic structure, defect density and photocatalytic consequences will be discussed.

## Experimental methods

### Nanocrystal preparation

Gallium-rich Cu-Ga-S ternary nanocrystals were prepared in a fume hood under inert conditions as follows: Typically, a mixture of 1.0 mmol of copper (II) acetylacetonate (Sigma-Aldrich,  $\geq 99.99\%$  trace metals basis) and the desired amount of gallium (III) acetylacetonate (i.e., 1, 3, or 5 mmol; Sigma-Aldrich,  $\geq 99.99\%$  trace metals basis), 3.5 mmol of trioctylphosphine oxide (90%, Aldrich, technical), and 15 mL of oleylamine (70%, Aldrich, technical grade) were placed in a four-neck, round-bottom flask and stirred at room temperature for 30 min with Ar purging. The solution was then heated to 120 °C and maintained at this temperature for 1 h to remove water. The temperature was then increased to 150 °C, and the desired amount of 1-dodecanethiol (i.e., 4, 10, or 16 mmol, Sigma-Aldrich) was rapidly injected into the solution under an Ar atmosphere with continuous stirring. The solution color changed from dark blue to shiny yellow. The temperature of the solution was maintained at 150 °C for 30 min before being gradually increased to 290 °C. After 5 h, the mixture was cooled, and the nanocrystals were isolated via centrifugation and thoroughly washed with an ethanol/hexane mixture (50% v/v). The particles were then dried in a vacuum oven at 45 °C. The zinc substituted in the gallium-rich Cu-Ga-S ternary nanocrystals were prepared by the same recipe, using the desired amount of zinc acetate ( $x = 0.3, 0.6, 0.7$  or  $0.9$  mmol; Sigma-Aldrich) and gallium (III) acetylacetonate ( $(5-(2/3)x = 4.8, 4.6, 4.53$  or  $4.4$  mmol). For convenience, the sample is designated as  $Zn_x\text{-CuGa}_5\text{S}_8$  with different  $x$  value of the precursor.

### Nanocrystal characterization

The XRD patterns of Cu-Ga-S ternary nanocrystals were collected on a Bruker D8 Advance diffractometer (DMAX 2500) operating with a  $\text{CuK}\alpha$  energy source at 40 kV and 40 mA. XPS analyses were performed on an AMICUS/ESCA 3400 KRATOS instrument equipped with Mg anodes at 12 kV and 10 mA. A prominent maximum peak of carbon (1s at 284.6 eV) was taken as the reference to calibrate the XPS spectra. High-resolution transmission electron microscopy (HRTEM) was performed at 300 kV on an instrument of the type, TITAN G<sup>2</sup> 80-300 ST from FEI Company. The selected area electron diffraction (SAED) patterns were obtained to determine the inter-planar d-spacings of the crystalline phases present in the samples. In addition, the Cu, Ga, and S elemental maps were also produced using a post-column energy-filter of model Tridium 863 from Gatan, Inc. These elemental maps were acquired from the Cu-M45, Ga-M45, and S-L23 edges of the Cu, Ga, and S elements, respectively. Moreover, the so-called 3-window method was employed to generate the elemental maps. Diffuse reflectance spectroscopy (DRS) was performed by employing a JASCO (V-670) spectrophotometer equipped with a 60 mm $\phi$  integrating sphere. A USRS-99-010 labsphere was employed as a reflectance standard. The reflectance spectra were converted to the absorbance mode using the Kubelka-Munk method. Photoluminescence (PL) spectra were measured using a Fluoromax-4 spectrofluorometer (HORIBA Scientific). For inductively coupled plasma-optical emission spectroscopy

(ICP-OES), analyses were accomplished by weighing ca. 12-15 mg of each sample and digesting it in a mixture of 3 mL of concentrated HCl and 1.0 mL of concentrated HNO<sub>3</sub>. After dilution to 50 mL, the ICP data were recorded on a Varian 715-ES device.

### Photocatalytic H<sub>2</sub> evolution activity measurements

The photocatalytic H<sub>2</sub> evolution assessment of the prepared nanomaterials was performed in a Pyrex top-irradiation reaction vessel connected to a glass closed-gas circulation system. In a typical run, 25 mg of the Cu-Ga-S ternary nanocrystals powder was dispersed in 25 mL of a 0.05 mol L<sup>-1</sup> Na<sub>2</sub>S/ 0.3 mol L<sup>-1</sup> Na<sub>2</sub>SO<sub>3</sub> aqueous solution by sonication. The suspension was subsequently poured into the photoreactor, and the desired amount of cocatalyst aqueous solution (RhCl<sub>3</sub>·xH<sub>2</sub>O, Rh 38-40%) was added. The photoreactor was then sealed and connected to the circulation system. After evacuating the photoreactor and introducing Ar several times, the photoreactor was irradiated using a 300 W Xe-arc lamp (MAX-303, Asahi Spectra: 58 mW cm<sup>-2</sup>, measured photon distribution is shown in Figure S1) equipped with an exchangeable band-pass filter (385–740 nm). For the apparent quantum efficiency measurements, the photocatalytic H<sub>2</sub> evolution rate was measured by employing a band-pass filter. The photon flux was measured using a spectroradiometer (EKO, LS-100). The apparent quantum efficiency was calculated as the rate of H<sub>2</sub> evolution ( $\mu\text{mol s}^{-1}$ ) multiplied by two, divided by the incident photon flux ( $\mu\text{mol s}^{-1}$ ).

### Computational details

Geometry optimizations were performed with the global hybrid functional PBE0<sup>33</sup> along with the *ab initio* CRYSTAL14 code<sup>34</sup>, using localized (Gaussian) basis sets and solving self-consistently the Hartree-Fock and Kohn-Sham equations thus allowing the efficient use of hybrid functionals. The basis set consists of six s, five p and two d shells (864111/64111/41) for Cu,<sup>35</sup> Ga,<sup>36</sup> and Zn,<sup>37</sup> and six s, five p and two d shells (863111/63111/41) for S. The reciprocal space was sampled with a 12×12×12 k-points mesh for the CuGaS<sub>2</sub> chalcopyrite and wurtzite and for the CuZn<sub>0.5</sub>Ga<sub>2</sub>S<sub>4</sub> structures. A 9×9×3 k-point mesh was used for the CuGa<sub>5</sub>S<sub>8</sub> and CuZn<sub>0.43</sub>Ga<sub>2.43</sub>S<sub>4.57</sub> compounds. The convergence criterion for the SCF cycle was fixed at 10<sup>-7</sup> Ha. All electronic properties were computed using the HSE06<sup>38,39</sup> exchange-correlation functional on top of the PBE0 geometry using the same computational parameters. This protocol based on geometry optimization with PBE0 and single points with HSE06 is inspired from ref.<sup>40,41</sup>

## Results and Discussion

Stoichiometric and gallium-rich ternary nanocrystals were synthesized via a facile hot injection method. The fast injection of 1-dodecanethiol into a mixture of Cu(acac)<sub>2</sub> and Ga(acac)<sub>3</sub> dissolved in oleylamine at 150 °C leads to formation of an intermediate complex and thus prevents the formation of binary compounds (e.g., CuS, Cu<sub>2</sub>S, and Ga<sub>2</sub>S<sub>3</sub>) upon raising the temperature from 150 to 290 °C, as evidenced by the XRD analysis. Moreover, the resultant XRD diffractogram presented in Figure 1 shows that the major peaks at 2 theta values match well with those of the wurtzite structure reported in the literature.<sup>42,43</sup> Based on the results, it can be concluded that the Cu-Ga-S nanocrystals are composed of metastable defected wurtzite rather than formation of the thermodynamically preferred chalcopyrite phase.<sup>45,46</sup> In fact, 1-dodecanethiol and

oleylamine are strong coordinating ligands and can bind to the surface of Cu–Ga–S nanocrystals and consequently decrease the surface energy for stabilizing the metastable wurtzite phase.<sup>43–46</sup> Such a ‘ligand effect’ as a structure-directing agent has been observed also in experimental studies of wurtzite CuInS<sub>2</sub> nanocrystal synthesis.<sup>47,48</sup>

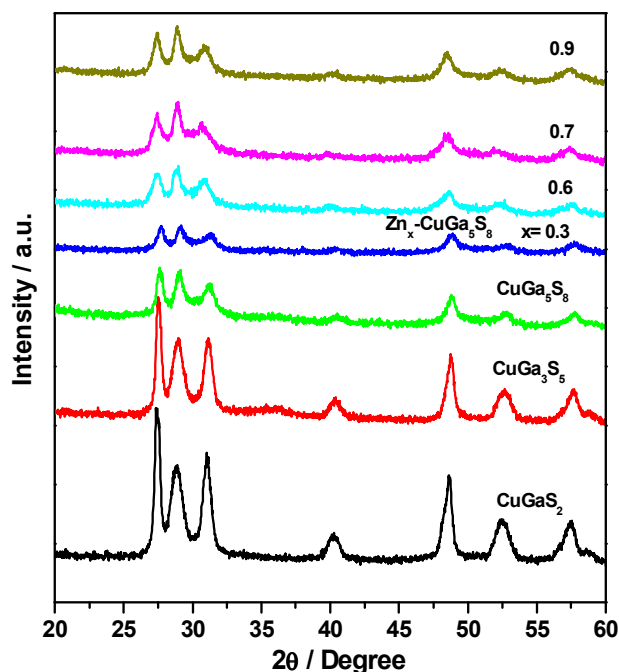


**Figure 1.** X-ray diffraction patterns of stoichiometric and gallium-rich Cu–Ga–S ternary nanocrystals and Zn<sub>x</sub>-CuGa<sub>5</sub>S<sub>8</sub>.

To prove the necessity of 1-dodecanethiol in the synthesis as a capping ligand and sulfur source, CuGa<sub>5</sub>S<sub>8</sub> was prepared employing solid sulfur dissolved in oleylamine as a sulfur source instead of 1-dodecanethiol under the same condition. XRD analysis of the obtained material indicated not a wurtzite structure but a defected chalcopyrite structure (Figure S2). This result demonstrates the crucial role of the capping ligand and of the nature of the sulfur source in controlling the crystal structure. In addition to the ligand effect, other factors such as the nature of the sulfur source and its decomposition rate might also be the reason for the formation of the metastable wurtzite structure, as previously encountered for CuInS<sub>2</sub>.<sup>49</sup> Figure 1 also shows that the substitution of zinc for Cu–Ga–S system does not alter the crystal structure, keeping the wurtzite structure.

The oxidation state of the Zn<sub>0.6</sub>-CuGa<sub>5</sub>S<sub>8</sub> surfaces was measured using X-ray photoelectron spectroscopy (XPS). Figure 2a shows the typical spectra for the monovalent Cu 2p core split into 2p<sub>3/2</sub> (932.6 eV) and 2p<sub>1/2</sub> (952.5 eV) peaks. The characteristic satellite peak associated with divalent Cu 2p<sub>3/2</sub> at ca. 942 eV does not appear, indicating that these peaks can unambiguously be assigned to the Cu<sup>+</sup> state. The Cu<sup>+</sup> peaks are in good agreement with those observed for ternary and quaternary metal sulfide nanocrystals.<sup>26,50,51</sup> Figure 2b shows the Ga 2p<sub>3/2</sub> core peak at 1118.5 eV, consistent with Ga<sup>3+</sup>.<sup>26</sup> Figure 2c shows the Zn 2p core split into 3p<sub>3/2</sub> (1022.2 eV) and 3p<sub>1/2</sub> (1044.3 eV) peaks, with a peak splitting of 23.1 eV, consistent with the standard splitting exhibited by divalent Zn.<sup>45</sup> The peak in Figure 2d, located at 161.7 eV, can be assigned to the S 2p binding energy with a valence of S<sup>2–</sup>.<sup>46</sup>

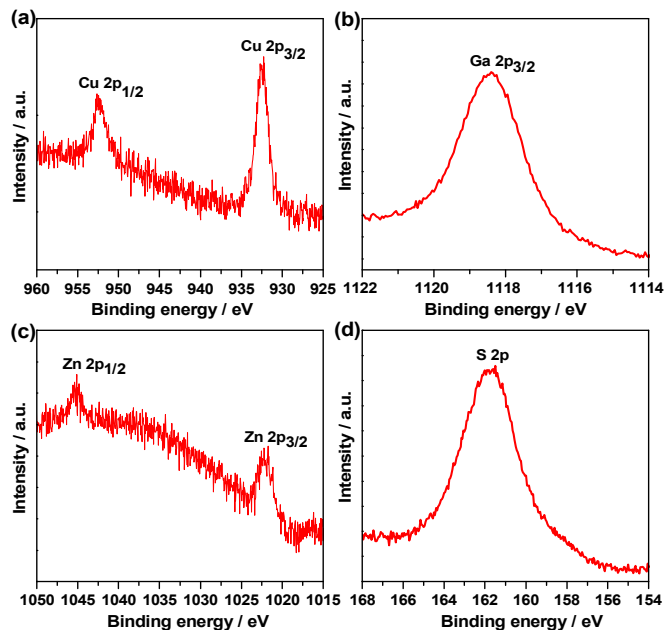


**Figure 2.** XPS spectra of Zn<sub>0.6</sub>-CuGa<sub>5</sub>S<sub>8</sub> nanocrystals.

Because copper, gallium, and zinc share the lattice sites in the wurtzite structure, the relative compositions of wurtzite Cu–Ga–S and Zn-substituted Cu–Ga–S ternary nanocrystals can widely vary. Consequently, the composition of the nanocrystals was analyzed by inductively coupled plasma atomic emission spectroscopy (ICP-OES). The expected and actual formulas of the synthesized Cu–Ga–S ternary nanocrystals are summarized in Table 1. The results showed that the stoichiometric CuGaS<sub>2</sub> was successfully obtained. In fact, the common formula Cu<sup>I</sup>B<sup>III</sup>C<sup>VI</sup><sub>2</sub> is only valid for stoichiometric compounds where the Cu:Ga ratio is 1:1.<sup>26,29</sup> To synthesize the gallium-rich wurtzite Cu–Ga–S ternary nanocrystals, Cu:Ga ratios targeting 1:3 and 1:5 gave an average Cu:Ga composition of 1:2.1 and 1:4.1, respectively. The gallium-rich ternary Cu–Ga–S with the formula CuGa<sub>2.1</sub>S<sub>3.7</sub> and CuGa<sub>4.1</sub>S<sub>6.7</sub> were obtained (these actual formula are used hereafter). The zinc substituted sample (targeting x = 0.6) gave a composition of CuZn<sub>0.6</sub>Ga<sub>3.8</sub>S<sub>6.8</sub>. For simplicity, the Zn-substituted nanocrystals are designated as Zn<sub>x</sub>-CuGa<sub>5</sub>S<sub>8</sub> with different x value of the precursor through the paper.

**Table 1.** Composition (as determined by ICP-OES analysis) of bare and zinc-substituted Cu–Ga–S ternary nanocrystals isolated after aging at 290 °C for 5 h.

Nanocrystals (expected formula)	Measured molar ratio of			Nanocrystals (actual formula)
	Cu/Cu	Ga/Cu	Zn/Cu	
CuGaS <sub>2</sub>	1.0	1.0		CuGaS <sub>2</sub>
CuGa <sub>3</sub> S <sub>5</sub>	1.0	2.1		CuGa <sub>2.1</sub> S <sub>3.7</sub>
CuGa <sub>5</sub> S <sub>8</sub>	1.0	4.1		CuGa <sub>4.1</sub> S <sub>6.7</sub>
Zn <sub>0.6</sub> -CuGa <sub>5</sub> S <sub>8</sub>	1.0	3.8	0.6	CuZn <sub>0.6</sub> Ga <sub>3.8</sub> S <sub>6.8</sub>

The morphology of some of the prepared Cu–Ga–S ternary nanocrystals was investigated using high-resolution transmission electron microscopy (HR-TEM). Figure 3a displays the image of the CuGa<sub>4.1</sub>S<sub>6.7</sub> nanocrystals at low magnification. The image indicates the successful formation of nanocrystals with rather random size distribution of a diameter up to 25 nm. The HR-TEM images of single particles (Figure 3b and 3c) and the selective area electron diffraction (SAED, inset Figure 3c) reveal well-resolved (100) wurtzite-specific

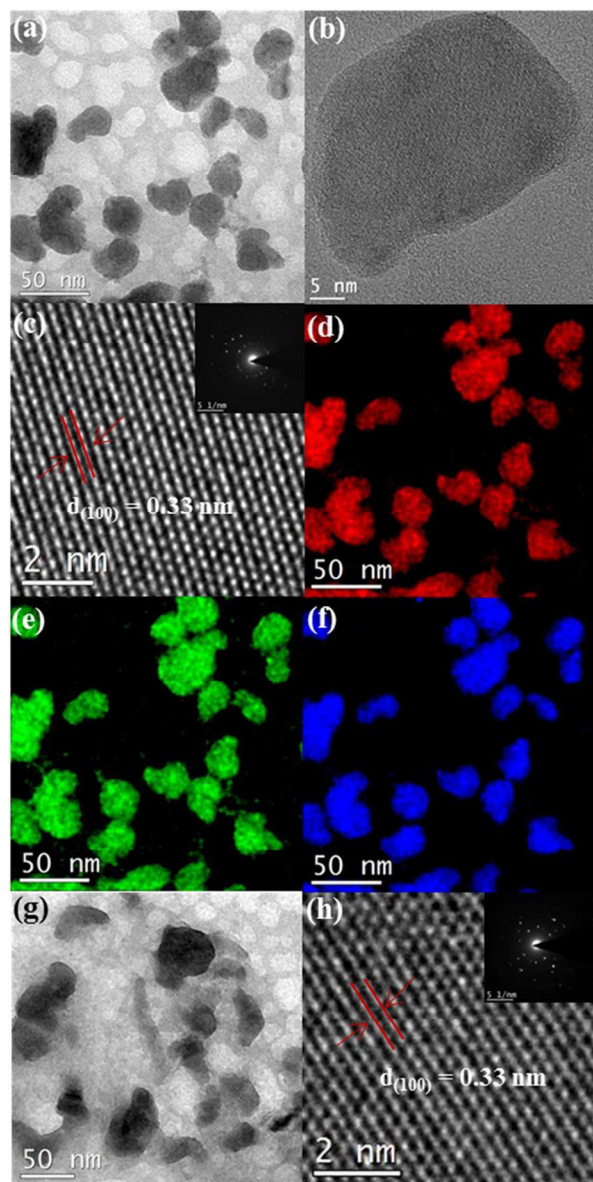


**Figure 3.** HR-TEM images of  $\text{CuGa}_{4.1}\text{S}_{6.7}$  nanocrystals at low (a) and high (b,c) magnification. EFTEM elemental maps of Cu (d), Ga (e), and S (f); (g) and (h): low and high magnification HR-TEM images of  $\text{Zn}_{0.6}\text{-CuGa}_5\text{S}_8$  nanocrystals. The inset of the (c) and (h) images display the SAED patterns.

lattice planes ( $d = 0.33$  nm) and diffraction spots indicative of the highly crystalline nature of the Cu–Ga–S nanocrystals. These results are consistent with the XRD analysis, confirming that the obtained nanocrystals exhibit a wurtzite structure. The elemental mapping can provide information on the spatial distribution of different compositional elements in Cu–Ga–S ternary nanocrystals. Figure 3d, 3e, and 3f show the energy-filtered TEM (EFTEM) elemental maps of Cu, Ga, and S. The findings clearly illustrate that the spatial distribution of compositional elements in the  $\text{CuGa}_{4.1}\text{S}_{6.7}$  nanocrystals is uniform. The morphology of the zinc-substituted gallium-rich Cu–Ga–S nanocrystals, i.e.,  $\text{Zn}_{0.6}\text{-CuGa}_5\text{S}_8$ , has also been investigated. In general, a similar morphology to that of the  $\text{CuGa}_{4.1}\text{S}_{6.7}$  nanocrystals was also observed (Figure 3g); however, substitution of zinc in the  $\text{CuGa}_{4.1}\text{S}_{6.7}$  nanocrystals apparently makes the particles shape more irregular. The

morphology variation with zinc substitution is likely caused by differences in the binding strength of the respective cations with ligands. The HR-TEM image of a single particle (Figure 3h) and the selective area electron diffraction (SAED, inset Figure 3h) demonstrate well-resolved (100) wurtzite-specific lattice planes ( $d = 0.33$  nm) and diffraction spots that are also indicative of the highly crystalline nature of the  $\text{Zn}_{0.6}\text{-CuGa}_5\text{S}_8$  nanocrystals. EFTEM elemental mapping of Cu, Ga, Zn, and S indicates that these elements are uniformly distributed in the nanocrystals (Figure S3).

The optical properties and bandgap of the as-prepared stoichiometric and gallium-rich Cu–Ga–S nanocrystals, as well as the zinc-substituted gallium-rich Cu–Ga–S nanocrystals, were determined by UV-Vis diffuse reflectance spectroscopy (DRS). As shown in Figure 4, the onset of the Kubelka-Munk function is more or less the same for the bare and zinc-substituted gallium-rich Cu–Ga–S nanocrystals, evidencing that the zinc substitution in the gallium-rich Cu–Ga–S nanocrystals does not significantly shift the conduction band edge, assuming that the valence bands originating from the S and Cu orbitals overlap and remain constant. The stoichiometric  $\text{CuGaS}_2$  shows a stepwise increase of the Kubelka-Munk function, which indicates the existence of defects within the bandgap. From the onset of the absorption, the bandgap was calculated and found to be ca. 2.3 eV.

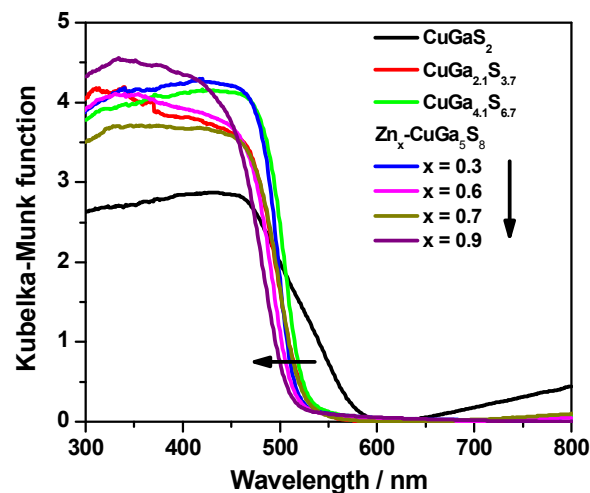


**Figure 4.** Diffuse reflectance spectra of stoichiometric and gallium-rich Cu–Ga–S ternary nanocrystals and Zn substituted Cu–Ga–S.

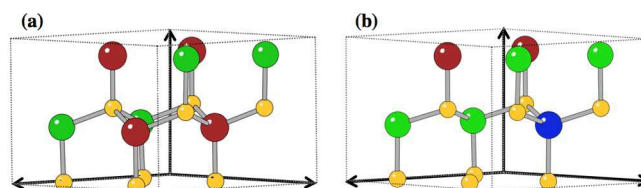


**Figure 5.** Unit cells of (a) wurtzite  $\text{CuGaS}_2$  and (b) wurtzite  $\text{CuZn}_{0.5}\text{Ga}_2\text{S}_4$ .

DFT calculations were performed to get insight in the electronic structure of Cu–Ga–(Zn)–S and to support the observation of UV-Vis measurements. In supporting information, a detailed explanation of the protocol used to build the  $\text{CuGaS}_2$  wurtzite based structures is presented. The unit cell designed for the wurtzite  $\text{CuGaS}_2$  and  $\text{CuZn}_{0.5}\text{Ga}_2\text{S}_4$  systems is

presented in Figure 5. To our best knowledge, no theoretical work has been published on the electronic structure calculation of wurtzite  $\text{CuGaS}_2$  except for the one of Xiao *et al.* that predicts a metallic behavior in opposition to experimental results.<sup>29</sup>

It is interesting to compare the electronic structure of the wurtzite and the chalcopyrite polymorphs of  $\text{CuGaS}_2$ , the latter form being the thermodynamically stable phase of  $\text{CuGaS}_2$  at room temperature and atmospheric pressure. The computed and experimental bandgaps of the two structures are gathered in Table 2. DFT calculations confirm the bandgap reduction going from the chalcopyrite to the wurtzite form of  $\text{CuGaS}_2$ . Furthermore, the band structure calculation on the wurtzite structure (Figure 6) indicates that the bandgap is direct (at the  $\Gamma$  point), as for the chalcopyrite structure, leading to probably high absorption coefficient. Our results differ from the ones of Xiao *et al.* (performed with plane waves basis set and PBE functional) since we reproduce the semiconductor nature of the wurtzite  $\text{CuGaS}_2$ , with a bandgap in agreement with the experiment.<sup>29</sup> The computed density of states of the wurtzite  $\text{CuGaS}_2$  is presented in Figure 7a. The valence and conduction bands have the same nature for the wurtzite and the chalcopyrite structures (see supporting information). The valence band is a combination of Cu and S orbitals, characterizing the strong covalency of the Cu-S bond. The conduction band is a combination of Ga and S orbitals and it shows a large dispersion. It is interesting to note that the change of the crystal structure for  $\text{CuGaS}_2$  (chalcopyrite-wurtzite) leads to almost unchanged electronic properties (band structure, density of states) probably because the local environment of the atoms remains identical. The only notable difference is for the bandgap, which is lower in the wurtzite structure than in the chalcopyrite one. This is comparable to the rutile and anatase forms of  $\text{TiO}_2$  that have very similar electronic structure but a slightly different bandgap.

**Table 2.** Experimental and computed bandgaps of  $\text{CuGaS}_2$ .

	Chalcopyrite	Wurtzite
Experimental	2.43 eV	2.20 eV
DFT HSE-06	2.46 eV	2.13 eV

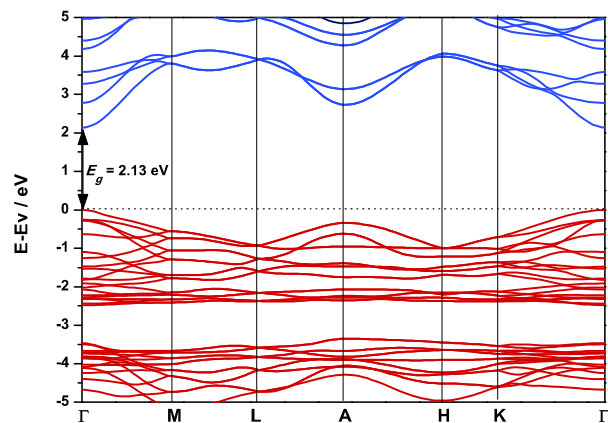


**Figure 6.** Computed band structure of the wurtzite  $\text{CuGaS}_2$  along with the HSE06 functional. Blue and red bands correspond to empty and filled bands, respectively.

Next, to analyze the influences of the increase of Ga/Cu ratio and of the Zn substitution, the electronic structures of the  $\text{CuGa}_5\text{S}_8$ ,  $\text{CuZn}_{0.5}\text{Ga}_2\text{S}_4$  and  $\text{CuZn}_{0.43}\text{Ga}_{2.43}\text{S}_{4.57}$  solids were computed. While the bandgap of  $\text{CuZn}_{0.43}\text{Ga}_{2.43}\text{S}_{4.57}$  gave a

value similar to the pure wurtzite structure, the bandgaps of the other two compounds were computed larger (see Table 3) in agreement with experimental observation (Figure 4). This bandgap enlargement results from an increase of the conduction band energy level. Since the conduction band is mainly located on Ga orbitals, this observation reveals that Ga electronic structure is more affected than copper one by Zn substitution and increase of Ga concentration. Interestingly, Zn atoms do not modify the nature of the valence and conduction bands that remain originated from Cu and Ga orbitals (in combination with S orbitals), respectively (see the DOS of  $\text{CuZn}_{0.5}\text{Ga}_2\text{S}_4$  in Figure 7b). In addition, neither Zn substitutions nor Cu vacancies create defect states inside the bandgap that could lead to recombination centers (all the DOS are presented in supplementary information). Furthermore, the band structure calculations (not shown) reveal that the direct nature of the bandgap is never affected by Zn substitution or Ga/Cu ratio increase. This is in agreement with experimental UV-Vis measurements that always reveal a marked absorption onset, suggesting an intense absorption coefficient.

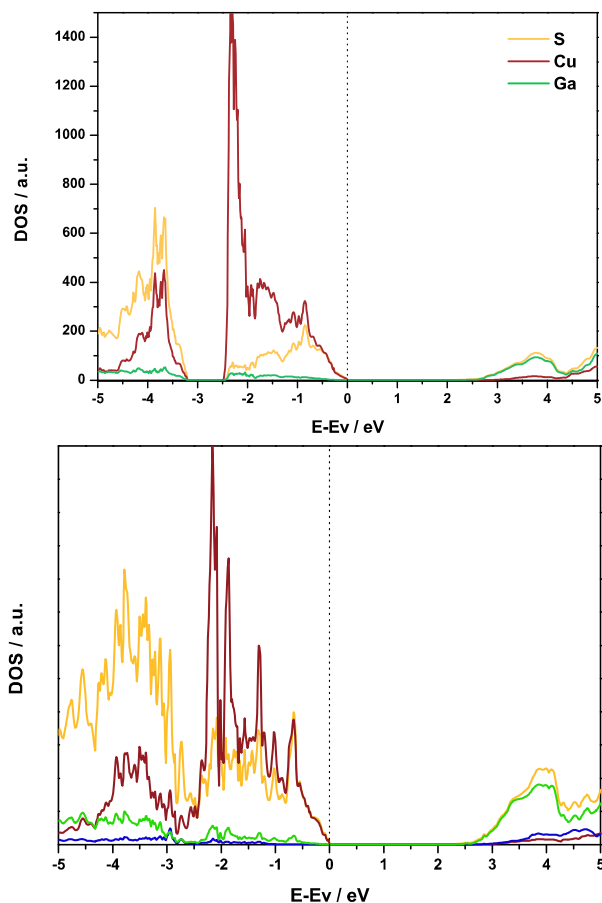


**Figure 7.** Computed density of states of the wurtzite (a)  $\text{CuGaS}_2$  and (b)  $\text{CuZn}_{0.5}\text{Ga}_2\text{S}_4$  along with the HSE06 functional. Yellow, red, green and blue lines correspond to the projection of the density of states on the S, Cu, Ga and Zn atoms, respectively.

**Table 3.** Computed bandgap (in eV) for all the simulated wurtzite structure based compounds.

	$\text{CuGaS}_2$	$\text{CuGa}_5\text{S}_8$	$\text{CuZn}_{0.5}\text{Ga}_2\text{S}_4$	$\text{CuZn}_{0.43}\text{Ga}_{2.43}\text{S}_{4.57}$
DFT	2.13	2.30	2.29	2.13

The photocatalytic activities of the prepared materials were assessed by measuring the photocatalytic H<sub>2</sub> evolution from Na<sub>2</sub>S/Na<sub>2</sub>SO<sub>3</sub> aqueous solutions. The bare Cu–Ga–S nanocrystals (without cocatalyst modification) exhibited negligible photocatalytic H<sub>2</sub> evolution activity. The loading of a small amount of noble metals promotes the photocatalytic H<sub>2</sub> evolution by creating electron sinks that facilitate photogenerated electron-hole pair separation.<sup>10</sup> Figure S4 shows the photocatalytic results using different metal cocatalysts (Rh, Ru, Pd, Pt). The presence of all the noble metals improved photocatalytic activity of wurtzite Cu–Ga–S system, likely minimizing overpotential for hydrogen evolution.<sup>2</sup> In our study, Rh was found to be most active, probably as a consequence of beneficial effects from both low barrier for the carriers at interface between metal and semiconductor, and low overpotential for the catalysis (H<sub>2</sub> evolution). The reaction without sulfide ions did not produce any H<sub>2</sub>, indicating that remaining ligands, if any, do not act as sacrificial reagent. In the presence of S<sup>2-</sup>, rapid ligand exchange with this ion is well known,<sup>52,53</sup> and therefore the effects of remaining ligands are considered to be minimal for the following photocatalytic reactions. Figure 8 presents the time course of the photocatalytic H<sub>2</sub> evolution on 0.5 wt.% Rh loaded stoichiometric and gallium-rich Cu–Ga–S ternary nanocrystals and Zn<sub>x</sub>-CuGa<sub>5</sub>S<sub>8</sub>. As shown in Figure 8, the stoichiometric Cu–Ga–S ternary nanocrystals exhibit no activity for photocatalytic H<sub>2</sub> production. Gallium-rich Cu–Ga–S ternary nanocrystals (CuGa<sub>2.1</sub>S<sub>3.7</sub>) showed higher activity than that of CuGa<sub>4.1</sub>S<sub>6.7</sub>. Zn<sub>0.6</sub>-CuGa<sub>5</sub>S<sub>8</sub> nanocrystals enhanced the photocatalytic activity by a factor of 5.

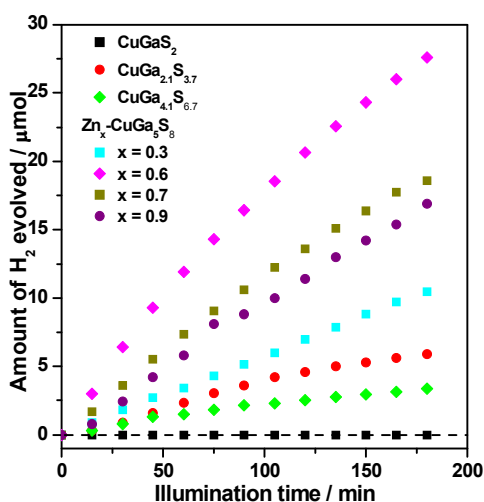


**Figure 8.** Time courses of photocatalytic H<sub>2</sub> evolution on stoichiometric and gallium-rich Cu–Ga–S ternary nanocrystals and Zn<sub>x</sub>-CuGa<sub>5</sub>S<sub>8</sub> loaded with 0.5 wt.% Rh from an aqueous Na<sub>2</sub>S (0.05 mol L<sup>-1</sup>)/Na<sub>2</sub>SO<sub>3</sub> (0.3 mol L<sup>-1</sup>) solution under visible-light illumination (λ 385–740 nm).

To further characterize the effects of Zn substitution into Cu–Ga–S system, the photoluminescence (PL) spectra of the different nanocrystals were also measured. Since the PL originates from the radiative recombination of the trapped photogenerated carriers, its intensity should have a strong correlation with the density of the defected states and thus with the photocatalytic H<sub>2</sub> evolution. The PL spectra are presented in Figure 9. The PL spectra were dominated by a broad

luminescence band close to the bandgap. The substitution of zinc in the gallium-rich Cu–Ga–S nanocrystals, i.e., CuGa<sub>4.1</sub>S<sub>6.7</sub>, leads to an increase of its PL intensity to some extent, and then the PL intensity was progressively decreased at a higher concentration of zinc. Interestingly, photocatalytic activity (Figure 8) and PL intensity correlates (Figure 9) very well, as depicted in Figure 10. The PL may arise from both bulk and surface contributions. In terms of bulk contribution, Zn substitution would lead to control stoichiometric ratios within Cu<sup>I</sup>-Zn<sup>II</sup>-Ga<sup>III</sup> sulfide by changing the cation (and accordingly anion) valences. Note that the decrease in the PL intensity, at a higher zinc concentration than x = 0.6, is attributed to non-radiative recombination of the trapped photogenerated charge carriers. Elimination of other recombination pathways where Zn may compensate the cationic vacancy by substituting Cu with Zn are proposed for the improvement for other sulfide systems.<sup>32,54</sup> Considering the surface contribution, the Zn-substitution somehow enhanced the surface defects where the excited electrons are directed to such sites, as claimed by Shi et al. for Zn<sub>x</sub>Cd<sub>1-x</sub>S system.<sup>28</sup> Once such surface sites where electrons migrate are well decorated with cocatalysts, the hydrogen evolution on these cocatalysts is effectively enhanced. It is difficult to pin down the reason at this stage, but the good correlation between H<sub>2</sub> activity and PL intensity is interesting observation for the future study.

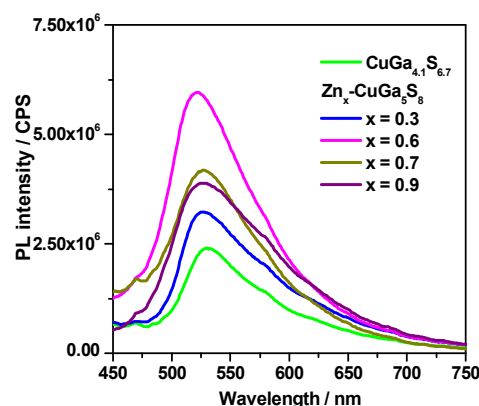


**Figure 9.** Photoluminescence spectra of Zn<sub>x</sub>-CuGa<sub>5</sub>S<sub>8</sub> nanocrystals. The excitation wavelength was 400 nm.

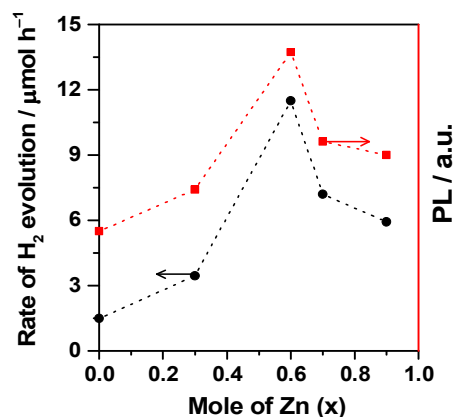


**Figure 10.** Relation between the mole of Zn<sub>x</sub>-CuGa<sub>5</sub>S<sub>8</sub> and the PL intensity (without cocatalyst loading) and rate of H<sub>2</sub> hydrogen evolution (with 0.5 wt% Rh).

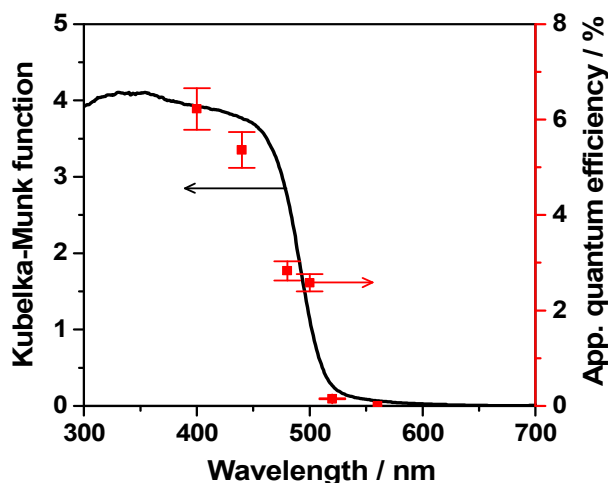


**Figure 11.** Diffuse reflectance spectrum of the 0.5 wt.% Rh-loaded  $\text{Zn}_{0.6}\text{-CuGa}_5\text{S}_8$  photocatalyst and the action spectrum of  $\text{H}_2$  evolution from an aqueous  $\text{Na}_2\text{S}$  ( $0.05 \text{ mol L}^{-1}$ )/ $\text{Na}_2\text{SO}_3$  ( $0.3 \text{ mol L}^{-1}$ ) solution.

To prove that the photocatalytic  $\text{H}_2$  evolution reaction proceeds through bandgap excitation, the apparent quantum efficiencies of  $\text{H}_2$  evolution were measured using band pass filters (the photon distributions are demonstrated in Figure S1). Figure 11 displays the diffuse reflectance and the action spectra of  $\text{H}_2$  evolution over 0.5 wt.% Rh-loaded  $\text{Zn}_{0.6}\text{-CuGa}_5\text{S}_8$  photocatalyst from an aqueous  $\text{Na}_2\text{S}$  ( $0.05 \text{ mol L}^{-1}$ )/ $\text{Na}_2\text{SO}_3$  ( $0.3 \text{ mol L}^{-1}$ ) solution. The onset of the action spectrum was in good agreement with the diffuse reflectance spectrum, indicating that the photocatalytic  $\text{H}_2$  evolution indeed proceeds through bandgap excitation. Moreover, the 0.5 wt.% Rh-loaded  $\text{Zn}_{0.6}\text{-CuGa}_5\text{S}_8$  photocatalyst exhibited a photocatalytic response toward  $\text{H}_2$  evolution up to 520 nm and exhibited ca.  $5.5 \pm 0.4\%$  apparent quantum efficiencies at 440 nm. For long-term illumination under solar simulator for 24 h (Figure S5), the amount of hydrogen reached  $\sim 700 \mu\text{mol}$ , but the evolution rate decreased from 50 to  $25 \mu\text{mol h}^{-1}$ . Although the presence of  $\text{S}^{2-}$  ions is effective to avoid photocorrosion,<sup>5,6</sup> the improved stability is desired, leaving a task for the future work.

## Conclusions

Cu–Ga–S nanocrystals were synthesized at different Cu/Ga ratios with a metastable wurtzite structure via a facile solution-based hot injection method using 1-dodecanethiol as a sulfur source. As a result, stoichiometric  $\text{CuGaS}_2$  and gallium-rich samples ( $\text{CuGa}_{2.1}\text{S}_{3.7}$  and  $\text{CuGa}_{4.1}\text{S}_{6.7}$ ), as well as Zn-substituted Cu–Ga–S were synthesized in the average size of  $\sim 25 \text{ nm}$ . Employing 1-dodecanethiol was found to be essential for stabilizing the metastable wurtzite structure. Zn substitution in Cu–Ga–S ternary compounds was found to improve considerably the efficiency of  $\text{H}_2$  evolution from an aqueous solution of  $\text{Na}_2\text{S}/\text{Na}_2\text{SO}_3$  solution. An optimum Zn substitution was determined, leading to a maximum photocatalytic efficiency. Interestingly, the PL measurements performed to understand the role of Zn substitution revealed that PL intensities followed the same trend that photocatalytic efficiencies although the reasons of these observations are still unclear. DFT calculations were performed on bulk semiconductors to understand all these findings. While these

calculations were able to reproduce the bandgap variation upon Ga/Cu ratio increase and Zn substitution, they revealed that the nature of band edges was not affected by Zn substitution. This result points out that the improvement of photocatalytic activities of these materials upon Zn substitution apparently does not come from bulk properties modifications but more probably from modified interface properties. On the sidelines of this work, DFT calculations were also the first ones to compute the electronic structure of the wurtzite  $\text{CuGaS}_2$  in agreement with experimental observations. The HSE06 functional was able to reproduce accurately the experimental bandgap variation from the chalcopyrite to the wurtzite structure of  $\text{CuGaS}_2$ . Finally, the highest  $\text{H}_2$  evolution was achieved by using 0.5 wt.% Rh/ $\text{Zn}_{0.6}\text{-CuGa}_5\text{S}_8$  photocatalyst with a quantum efficiency greater than 5% in the visible range.

## Acknowledgement

This work is supported by King Abdullah University of Science and Technology. A part of funding for this work was provided by Saudi Aramco under contract 6600024505/01. T.A.K. thanks the Chemistry Department Faculty of Science at Sohag University for granting him a leave of absence.

## Notes and references

- <sup>a</sup> Division of Physical Sciences and Engineering, KAUST Catalysis Center (KCC), King Abdullah University of Science and Technology (KAUST), 4700 KAUST, Thuwal 23955-6900, Saudi Arabia. E-mail: [kazuhiro.takanabe@kaust.edu.sa](mailto:kazuhiro.takanabe@kaust.edu.sa)  
<sup>b</sup> Department of Chemistry, Faculty of Science, Sohag University, Sohag 82524, Egypt.  
<sup>c</sup> Imaging and Characterization Lab, Abdullah University of Science and Technology (KAUST), Thuwal 23955-6900, Saudi Arabia.  
<sup>d</sup> Université de Lyon, Université Claude Bernard Lyon1, ENS Lyon, Centre National de Recherche Scientifique, 46 allée d'Italie, 69007 Lyon Cedex 07, France.

Electronic Supplementary Information (ESI) available: [Experimental and theoretical details]. See DOI: 10.1039/b000000x/

1. A. Kudo and Y. Miseki, *Chem. Soc. Rev.*, 2009, **38**, 253-278.
2. K. Takanabe and K. Domen, *Green*, 2011, **1**, 313-322.
3. F. E. Osterloh, *Chem. Soc. Rev.*, 2013, **42**, 2294-2320.
4. M. Tabata, K. Maeda, T. Ishihara, T. Minegishi, T. Takata and K. Domen, *J. Phys. Chem. C*, 2010, **114**, 11215-11220.
5. R. Williams, *J. Chem. Phys.*, 1960, **32**, 1505-1514.
6. N. Bühler, K. Meier and J. F. Reber, *J. Phys. Chem.*, 1984, **88**, 3261-3268.
7. N. M. Dimitrijevic, S. Li and M. Graetzel, *J. Am. Chem. Soc.*, 1984, **106**, 6565-6569.
8. M. Matsumura, S. Furukawa, Y. Saho and H. Tsubomura, *J. Phys. Chem.*, 1985, **89**, 1327-1329.
9. M. Barbeni, E. Pelizzetti, E. Borgarello, N. Serpone, M. Grätzel, L. Balducci and M. Visca, *Int. J. Hydrogen Energy*, 1985, **10**, 249-253.
10. M. Matsumura, T. Uchihara, K. Hanafusa and H. Tsubomura, *J. Electrochem. Soc.*, 1989, **136**, 1704-1709.
11. G. Ma, H. Yan, J. Shi, X. Zong, Z. Lei and C. Li, *J. Catal.*, 2008, **260**, 134-140.
12. H. Yan, J. Yang, G. Ma, G. Wu, X. Zong, Z. Lei, J. Shi and C. Li, *J. Catal.*, 2009, **266**, 165-168.
13. J. Yu, J. Zhang and M. Jaroniec, *Green Chem.*, 2010, **12**, 1611-1614.
14. K. Zhang and L. Guo, *Catal. Sci. Technol.*, 2013, **3**, 1672-1690.
15. Q. Li, H. Meng, P. Zhou, Y. Zheng, J. Wang, J. Yu and J. Gong, *ACS Catal.*, 2013, **3**, 882-889.
16. Q. Li, H. Meng, J. Yu, W. Xiao, Y. Zheng and J. Wang, *Chem. Eur. J.*, 2014, **20**, 1176-1185.
17. W. Yu, T. Isimjan, S. Del Gobbo, D. H. Anjum, S. Abdel-Azeim, L. Cavallo, A. T. Garcia-Esparza, K. Domen, W. Xu and K. Takanabe, *ChemSusChem*, 2014, **7**, 2575-2583.

18. M. Kokta, J. R. Carruthers, M. Grasso, H. M. Kasper and B. Tell, *J. Electr. Mater.*, 1976, **5**, 69-89.
19. I. Tsuji, H. Kato, H. Kobayashi and A. Kudo, *J. Am. Chem. Soc.*, 2004, **126**, 13406-13413.
20. I. Tsuji, H. Kato and A. Kudo, *Angew. Chem. Int. Ed.*, 2005, **117**, 3631-3634.
21. I. Tsuji, H. Kato and A. Kudo, *Chem. Mater.*, 2006, **18**, 1969-1975.
22. T. Pons, E. Pic, N. Lequeux, E. Cassette, L. Bezdetnaya, F. Guillemin, F. Marchal and B. Dubertret, *ACS Nano*, 2010, **4**, 2531-2538.
23. C. Sun, J. S. Gardner, G. Long, C. Bajracharya, A. Thurber, A. Punnoose, R. G. Rodriguez and J. J. Pak, *Chem. Mater.*, 2010, **22**, 2699-2701.
24. I. Tsuji, Y. Shimodaira, H. Kato, H. Kobayashi and A. Kudo, *Chem. Mater.*, 2010, **22**, 1402-1409.
25. H. Kaga, K. Saito and A. Kudo, *Chem. Commun.*, 2010, **46**, 3779-3781.
26. H.-T. Tung, Y. Hwu, I.-G. Chen, M.-G. Tsai, J.-M. Song, I. M. Kempson and G. Margaritondo, *Chem. Commun.*, 2011, **47**, 9152-9154.
27. Y.-H. A. Wang, X. Zhang, N. Bao, B. Lin and A. Gupta, *J. Am. Chem. Soc.*, 2011, **133**, 11072-11075.
28. J. Shi, H. Cui, Z. Liang, X. Lu, Y. Tong, C. Su and H. Liu, *Energy Environ. Sci.*, 2011, **4**, 466-470.
29. N. Xiao, L. Zhu, K. Wang, Q. Dai, Y. Wang, S. Li, Y. Sui, Y. Ma, J. Liu, B. Liu, G. Zou and B. Zou, *Nanoscale*, 2012, **4**, 7443-7447.
30. D. Aldakov, A. Lefrancois and P. Reiss, *J. Mater. Chem. C*, 2013, **1**, 3756-3776.
31. T. A. Kandiel, D. H. Anjum and K. Takanabe, *ChemSusChem*, 2014, **7**, 3112-3121.
32. H. Kaga and A. Kudo, *J. Catal.*, 2014, **310**, 31-36.
33. C. Adamo and V. Barone, *J. Chem. Phys.*, 1999, **110**, 6158-6170.
34. R. Dovesi, R. Orlando, A. Erba, C. M. Zicovich-Wilson, B. Civalleri, S. Casassa, L. Maschio, M. Ferrabone, M. De La Pierre, P. D'Arco, Y. Noël, M. Causà, M. Rérat and B. Kirtman, *Int. J. Quantum Chem.*, 2014, **114**, 1287-1317.
35. K. Doll and N. M. Harrison, *Chem. Phys. Lett.*, 2000, **317**, 282-289.
36. R. Pandey, J. E. Jaffe and N. M. Harrison, *J. Phys. Chem. Solids*, 1994, **55**, 1357-1361.
37. J. E. Jaffe, A.C. Hess, *Phys. Rev. B* 1993, **48**, 7903
37. T. Bredow, P. Heitjans and M. Wilkening, *Phys. Rev. B*, 2004, **70**, 115111.
38. J. Heyd, G. E. Scuseria and M. Ernzerhof, *J. Chem. Phys.*, 2003, **118**, 8207-8215.
39. J. Heyd, G. E. Scuseria and M. Ernzerhof, *J. Chem. Phys.*, 2006, **124**, 219906.
40. T. Le Bahers, M. Rérat and P. Sautet, *J. Phys. Chem. C*, 2014, **118**, 5997-6008.
41. S. T. A. G. Melissen, F. Labat, P. Sautet and T. Le Bahers, *Phys. Chem. Chem. Phys.*, 2014, **17**, 2199-2209.
42. W. Schäfer and R. Nitsche, *Mater. Res. Bull.*, 1974, **9**, 645-654.
43. M. D. Regulacio, C. Ye, S. H. Lim, Y. Zheng, Q.-H. Xu and M.-Y. Han, *CrystEngComm*, 2013, **15**, 5214-5217.
44. S.-H. Chang, B.-C. Chiu, Z.-L. Gao, S.-L. Jheng and H.-Y. Tuan, *CrystEngComm*, 2014, **16**, 3323-3330.
45. K.-L. Ou, J.-C. Fan, J.-K. Chen, C.-C. Huang, L.-Y. Chen, J.-H. Ho and J.-Y. Chang, *J. Mater. Chem.*, 2012, **22**, 14667-14673.
46. Q. Li, C. Zou, L. Zhai, J. Shen, L. Zhang, H. Yu, Y. Yang, X. Chen and S. Huang, *J. Alloys Compd.*, 2013, **567**, 127-133.
47. D. Pan, L. An, Z. Sun, W. Hou, Y. Yang, Z. Yang and Y. Lu, *J. Am. Chem. Soc.*, 2008, **130**, 5620-5621.
48. M. E. Norako, M. A. Franzman and R. L. Brutchey, *Chem. Mater.*, 2009, **21**, 4299-4304.
49. C. Stephan, in Institut für Technologie E-I3, Freien Universität Berlin, Reports of the Helmholtz Centre Berlin, 2011, p. 213.
50. L. D. Partain, R. A. Schneider, L. F. Donaghey and P. S. McLeod, *J. Appl. Phys.*, 1985, **57**, 5056-5065.
51. J. Chang and E. R. Waclawik, *CrystEngComm*, 2013, **15**, 5612-5619.
52. A. Nag, M. V. Kovalenko, J.-S. Lee, W. Liu and B. Spokoyny, D. V. Talapin, *J. Am. Chem. Soc.*, 2011, **133**, 10612-10620.
53. H. Zhang, B. Hu, L. Sun, R. Hovden, F. W. Wise, D. A. Muller and R. D. Robinson, *Nano Lett.*, 2011, **11**, 5356-5361.
54. I. Tsuji, H. Kato, H. Kobayashi and A. Kudo, *J. Phys. Chem. B*, 2005, **109**, 7323-7329.